Acta Astronautica 93 (2014) 176–181

Contents lists available at SciVerse ScienceDirect

Acta Astronautica

journal homepage: www.elsevier.com/locate/actaastro

# Extension of the universal erosive burning law to partly symmetric propellant grain geometries

H.S. Mukunda [a], P.J. Paul [a], Afroz Javed [b], Debasis Chakraborty [b,*]

[a] Indian Institute of Science, Bangalore, Karnataka, India
[b] Defense Research and Development Laboratory, Hyderabad, Andhra Pradesh 500058, India

ARTICLE INFO

Available online 13 July 2013

*Keywords:*
Erosive burning
Finocyl grain
CFD

ABSTRACT

This paper aims at extending the universal erosive burning law developed by two of the present authors from axi-symmetric internally burning grains to partly symmetric burning grains. This extension revolves around three dimensional flow calculations inside highly loaded grain geometry and benefiting from an observation that the flow gradients normal to the surface in such geometries have a smooth behavior along the perimeter of the grain. These are used to help identify the diameter that gives the same perimeter the characteristic dimension rather than a mean hydraulic diameter chosen earlier. The predictions of highly loaded grains from the newly chosen dimension in the erosive burning law show better comparison with measured pressure–time curves while those with mean hydraulic diameter definitely over-predict the pressures.



## 1. Introduction

Two of the present authors (HSM and PJP) [1] presented a procedure based on non-dimensional considerations by which the data on erosive burning from more than ten investigators from different laboratories across the world on both double base and composite propellants could be brought into a simple relationship as

$$\eta = 1 + 0.023(g^{0.8} - g_{th}^{0.8})\mathcal{H}(g - g_{th}) \quad (1)$$

to within an accuracy of $\pm 10\%$. In the above equation, $\eta$ is the ratio of burn rate with lateral flow to that without any flow (the classical erosive burning ratio $= r/r_0$), $g$ is essentially the ratio of mass flux through the port to the mass efflux from the surface modified for size effects as $(G/\rho_p r_0)\,(\rho_p r_0 d_0/\mu)^{-0.125}$, where $G$ is the mass flux through the port, $\rho_p r_0$ is the non-erosive mass efflux from the surface, $g_{th}$ is the threshold value obtained from the plot of the data as 35 and $\mathcal{H}$ is the Heaviside step function that is introduced to indicate a critical flux below which there is no erosive burning. The basis of the equation is that fluid mechanics controls the erosive burning and while many details of the propellant like the composition, particle sizes in the case of heterogeneous propellants do matter with regard to the burn rate, the data from different sources has not shown any specificity on non-dimensional parameter plots. While one cannot intrinsically rule out the subsidiary effects, there was no specific trend in the data to suggest that. Earlier investigators used various dimensional parameters and missed out the principal effects even though the important effects are embedded in the equations that have been used for a long time. Hasegawa et al. [2] used X-ray absorption measurements for double slab motors (DSM) to get a curve fit for erosion law of the form given by Dickinson et al. [3]. Unfortunately, they have chosen to depart from dimensionless correlation above to a new correlation based on dimensional mass flux with inadequate justification. Because of this reason, they have used different constants for different size motors showing clearly inadequacy of the relationship that earlier literature is filled with. Recently, Topalian et al. [4] have chosen to study erosive burning in composite propellants ignoring the

* Corresponding author. Tel.: +91 4024583310; fax: +91 40 24340037.
*E-mail addresses:* debasis_cfd@drdl.drdo.in, debasis_drdl@yahoo.co.in (D. Chakraborty).

0094-5765/$ - see front matter © 2013 IAA Published by Elsevier Ltd. All rights reserved.
http://dx.doi.org/10.1016/j.actaastro.2013.07.017

**Nomenclature**

| | |
|---|---|
| $A_p$ | local port area |
| $G$ | mass flux through port |
| $\mathcal{H}$ | Heaviside step function |
| $P$ | grain perimeter |
| $Re_0$ | Reynolds number defined as $\rho_p r_0 d_0/\mu$ |
| $U_{av}$ | average axial velocity |
| $d_0$ | port diameter |
| g | modified mass flux ratio defined as $(G/\rho_p r_0)(\rho_p r_0 d_0/\mu)^{-0.125}$ |
| $g_{th}$ | threshold mass flux ratio (=35) |
| $\dot{m}$ | mass flow rate kg/s |
| $r$ | burn rate with lateral flow |
| $r_0$ | burn rate without lateral flow |
| $x$ | axial location |
| $\mu$ | coefficient of dynamic viscosity |
| $\eta$ | erosive burning ratio |
| $\rho$ | density of products of combustion |
| $\rho_p$ | propellant density |
| $\tau_w$ | wall shear stress |

underlying fundamental influence brought out in Mukunda and Paul[1] and seeking any possible deviations from the universal relationship. In fact, the comparisons in Ref. [4] are so limited that the data fit into the above correlation and no extra effects expected to be delineated in their work seem apparent.

In Eq. (1), the motor size effect comes in through the Reynolds number, $Re_0=\rho_p r_0 d_0/\mu$ with $d_0$ being chosen as the port diameter. This equation has been applied routinely to the design of highly loaded grains that have circular port and found to give predictions consistent with large size motor data from tests. When it is expected to be extended to more complex geometries, like star grains, one would normally use the hydraulic diameter given by $4A_p/P$, where $A_p$ is the port area and $P$ is the grain perimeter. This relationship was routinely used in propellant grain design at the defense laboratories. When this relationship was used for grain shapes having partly Finocyl shape [5], it *over-predicted* the pressure variation in the early part of the burn. Burn rate differences in a star point and recess locations of a star and other shapes have been discussed in Williams et al. [6]. This subject that has remained unaddressed till now because there has been no clear demand on these aspects from motor designers. It is the objective of this paper to address the complex flow through the slots of the grain and the central region that affect the heat flux to the grain in the interior regions through a rigorous calculation of three-dimensional internal flow through the grain and in this process, seek any possible revision of the universal burn rate law for non-axisymmetric shapes.

## 2. The motors studied

Two rocket motors are considered for the study here. Both have a cylindrical section towards the head end and a finocyl shape in the aft region. The details of the calculations of one motor are set out here. The results of the other motor are summarized. The details of the motors are shown in Table 1. The length-to-diameter ratio of the cylindrical portion is about 18 for the first motor and 26 for the second motor.

The first motor has a finocyl geometry whose cross section is shown towards the right side. The vertical lines drawn refer to the locations where the 3-d thermo-fluid information is extracted. As shown in Fig. 1 is another highly loaded grain with a strong possibility of erosive burning occurring in the cylindrical portion itself; it could also occur in the finocyl part.

## 3. The 3-d computational details

A symmetric geometry of 45° sector for Motor-1 has been considered for the simulation. The geometry with the boundary locations is shown in Fig. 2.

**Table 1**
Properties of the motors under study.

| Parameter | Motor-1 | Motor-2 |
|---|---|---|
| Motor length, m | 2.1 | 4.8 |
| Port diameter, m | 0.17 | Varies from 0.31 to 0.49 |
| Initial cylindrical segment, m | 1.37 | 3.48 |
| Finocyl transition zone, m | 0.18 | 0.26 |
| Number of webs in the finocyl | 4 | 8 |
| Finocyl minimum dia., m | 0.08 | 0.13 |
| Finocyl maximum dia., m | 0.17 | Varies from 0.28 to 0.37 |
| Throat diameter, mm | 45 | 176 |
| Burn rate at 7 MPa and pressure index, n | 6.5 mm/s and 0.25 | 19 mm/s and 0.38 |

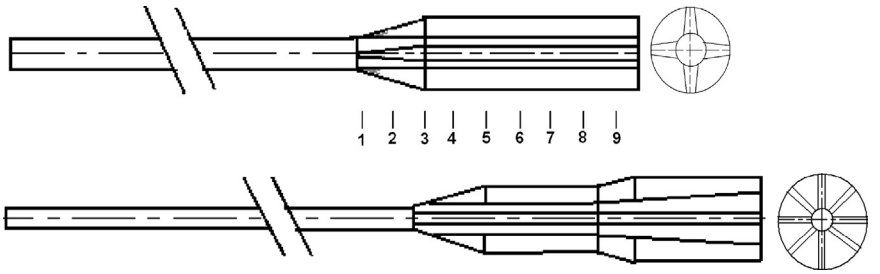


**Fig. 1.** Geometries of the two grains for Motor-1 (top) and Motor-2 (bottom); the first part is cylindrical and the aft part is finocyl with a transition region, the cross section shown on the right is of the aft end.

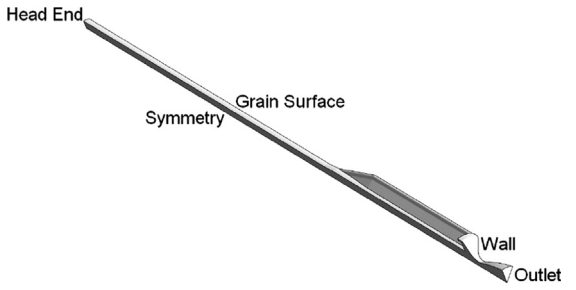


**Fig. 2.** Geometry of motor-1 for the simulation with the boundary locations.

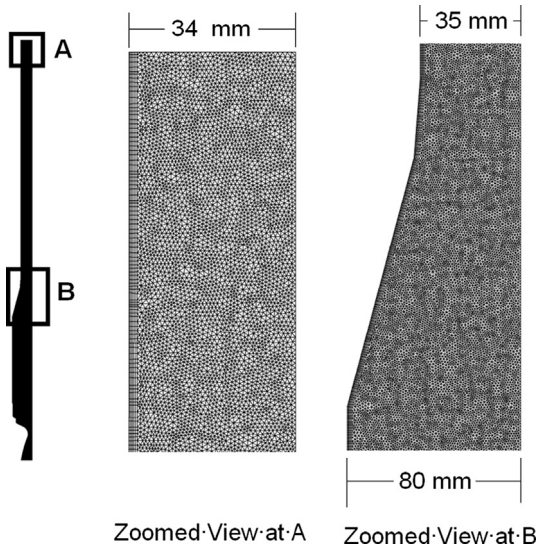


**Fig. 3.** Computational grid for the motor geometry.

**Table 2**
Geometrical properties and mass flow rates from different cross sections.

| Sl. no. | Axial location (m) | Perimeter (m) | Port area $\times 10^3$ ($m^2$) | Mass flow rate (kg/s) | Mass flux ($kg/m^2s$) |
|---|---|---|---|---|---|
| 1 | 1.37 | 0.24 | 4.49 | 3.20 | 710 |
| 2 | 1.43 | 0.35 | 5.33 | 3.41 | 640 |
| 3 | 1.53 | 0.52 | 7.53 | 3.89 | 520 |
| 4 | 1.63 | 0.54 | 7.84 | 4.48 | 570 |
| 5 | 1.73 | 0.54 | 7.88 | 5.05 | 640 |
| 6 | 1.82 | 0.54 | 7.92 | 5.60 | 710 |
| 7 | 1.91 | 0.55 | 7.96 | 6.15 | 770 |
| 8 | 2.01 | 0.55 | 8.01 | 6.76 | 840 |
| 9 | 2.08 | 0.55 | 8.04 | 7.14 | 890 |

Tetrahedral grids are made using ICEM CFD [7] package, a layer of hexahedral grids are used at walls and grain surface to resolve gradients. Three different grids of 0.74, 1.42, and 3.29 millions sizes with minimum normal grid spacing of 0.4, 0.1 and 0.01 mm are studied to establish the grid independence of the results. A typical grid is shown in Fig. 3. It can be observed that the grids near the geometrical changes are sufficiently clustered to capture high flow gradients expected in these regions. Minimum $y^+$ varies from head end to nozzle end and typical $y^+$ at head end and nozzle is of the order of 0.1 and 20, respectively.

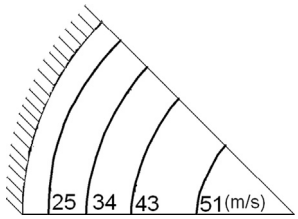


**Fig. 4.** The cross section of the propellant showing that at this section 0.44 m from the head end, the port is circular. Velocities are shown in on the contour lines. For instance contour line near the surface has a velocity of 25 m/s and contour close to the central region of the port has a velocity of 51 m/s.

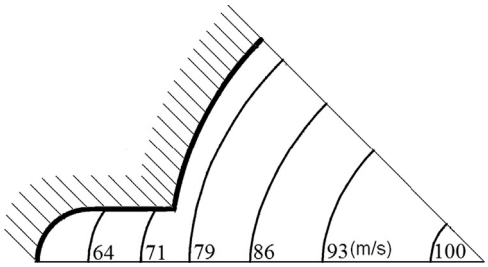


**Fig. 5.** The cross section of the propellant showing that at this section 1.43 m from the head end, the port is in transition to finocyl geometry.

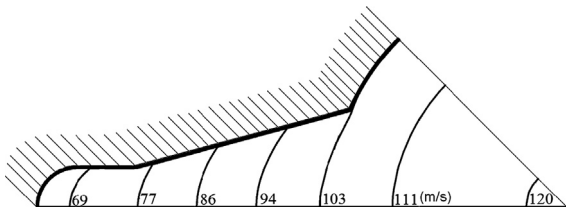


**Fig. 6.** The cross section of the propellant showing that at this section 1.91 m from the head end, the port is of finocyl geometry close to the nozzle end.

## 4. Flow simulation

The flow simulation is carried out using CFX11 commercial CFD solver [8]. It solves 3-D Navier–Stokes equations with $k$–$\varepsilon$ turbulence model. For the present simulations, the grain surface is set as isothermal wall at 2980 K temperature and the propellant mass flow from the grain is considered as the source term in the mass continuity equation. Two sides are taken as symmetry boundary conditions and the nozzle wall and head end wall are taken as no slip adiabatic walls. Supersonic outflow boundary condition is prescribed at the outlet as the flow at the nozzle exit is supersonic.

A second order numerical scheme is utilized for the simulations. A physical time step of 0.2 ms is used for the steady state simulations. The simulation is run till a convergence level of $1 \times 10^{-4}$ is reached on normalized logarithmic residuals.

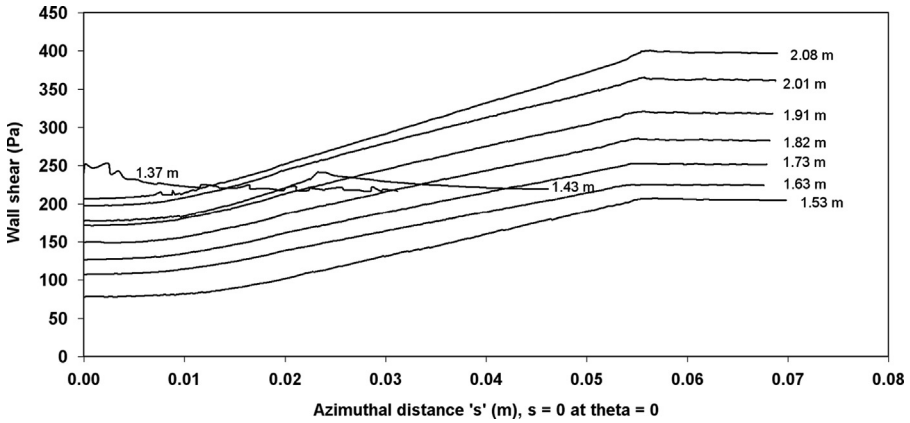


**Fig. 7.** The plot of wall shear stress along the grain surface with s, $\theta=0$ taken at the recess of the Finocyl. Note that the wall stress ($\tau_w$) increases from the recess to the Finocyl point closer to the center of the port.

The thermo chemical properties of the combustion gases used for the simulations are given as follows: Total temperature, ratio of specific heats, molecular weight, thermal conductivity and dynamic viscosity of the gases are 2980 K, 1.214, 25.1, 0.4058 W/m K, and $9.513\times10^{-5}$ Pa s, respectively. These quantities are evaluated using NASA CEA 600 program [9] for the propellant composition used in the motor.

## 5. Results and discussion

The geometrical properties and flow rates at various cross sections are set out in Table 2. The cylindrical portion of the grain extends up to 1.366 m, a transition to fin-*o*-cyl up to 1.532 m and then the fin-*o*-cyl geometry.

The velocity contours at a few cross sections are shown in Figs. 4–6.

Figs. 5 and 6 show that the velocities in the slot area are smaller than in the core as may be expected. Calculations of turbulent flow with fine resolution were used to evaluate the azimuthal variation of the wall stress at several sections along the axis. Fig. 7 shows the plot of wall shear stress ($\tau_w$) as obtained from the calculations plotted as a function of distance from the Finocyl recess to the region closer to the center of the port along the surface of the grain. Positions 1 and 2 correspond to the cylindrical region, position 3 to the transition region and positions 4 to 6 at distances towards the nozzle in the finocyl section.

A simple observation shows that in the Finocyl section, the stress seems to increase with axial distance over which the mass flow rates are also increasing. Further there seems to be a linear fall of stress over the Finocyl surface from the zone close to the center to the recess of the finocyl. A careful study of the relationships showed that a parameter $[2\tau_w/\rho U_{av}^2]$ $(P\,x/A_p]$ where $\rho U_{av}^2/2$ refers to the local dynamic pressure based on the average velocity, $U_{av}$, $P$=the perimeter of the cross section at distance $x$ from the head end and $A_p$ is the local port area may condense the data of several sections into a single line. This is shown in Fig. 8. All the data of five stations can be condensed into a single line $[2\tau_w/\rho U_{av}^2]$ $(P\,x/A_p]=0.6+0.5(R/R_{min})$ to within

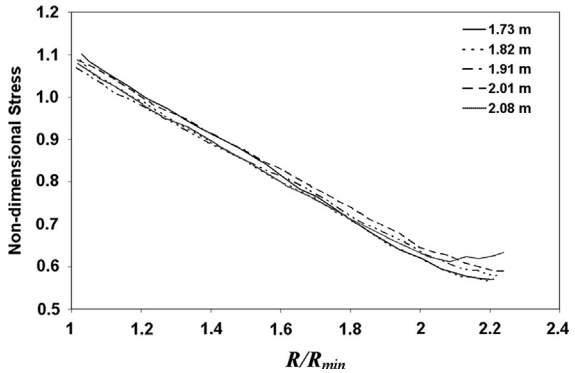


**Fig. 8.** The plot of non-dimensional stress $[2\tau_w/\rho U_{av}^2]$ $(P\,x/A_p]$ at several axial sections with the distance from the finocyl region closest to the center of the grain along the grain surface measured as distance from the center ($R_{min}$ is the minimum radial distance and it represents the finocyl region closest to the axis of the motor).

5%. The shear stress directly controls the heat transfer to the surface and hence the local burn rate along the surface. This implies that the burn rate in the recess region could be lower by 40% compared to that at the Finocyl region close to the center of the port. If we include the blocking effect the reduction of burn rate in the recess region could be lower by 20 to 25% compared that in the region closest to the center. If one desires to compute the precise geometry with time for erosive burning related ballistics, this information is of importance.

If it can be taken that erosive burning is dominant over small regions for the early part of the combustion process as it happens in practice, *a simpler procedure can indeed be evolved*. In this approach, it is taken that an average heat flux is assumed prevalent over the entire burning perimeter. The more appropriate characteristic dimension to choose for evaluating the size effect through $Re_0$ is defined in terms of perimeter as $P/\pi$ instead of $4A_p/P$. This will translate to $d_p$ for circular port cross section as is needed. Calculations have been made for the above geometry dominated by erosive burning. The results are presented below. The data for grain−1 are set out in Table 3.

**Table 3**
Geometric and flow properties along the motor length ($p_c$=70 atm, $T_c$=2800 K, $L_p$=characteristic length=perimeter/$\pi$, $d_h$=hydraulic diameter).

| $x$ m | $A_p$ cm$^2$ | $L_p$ m | $\dot{m}$ kg/s | $\rho_g$ kg/m$^3$ | $G/\rho_p r_0$ | $Re_r \times 10^4$ | $g(L_p)$ | $\eta$ | $g(d_h)$ | $\eta'$ |
|---|---|---|---|---|---|---|---|---|---|---|
| 0.44 | 35.6 | 0.067 | 1.01 | 7.68 | 21.8 | 1.46 | 15.6 | 1.0 | 15.6 | 1.0 |
| 0.88 | 35.9 | 0.067 | 1.98 | 7.64 | 42.3 | 1.46 | 30.3 | 1.0 | 30.3 | 1.0 |
| 1.43 | 53.3 | 0.112 | 3.3 | 7.58 | 47.5 | 2.44 | 31.9 | 1.0 | 34.5 | 1.0 |
| 1.73 | 78.8 | 0.173 | 4.9 | 7.55 | 47.7 | 3.75 | 30.3 | 1.0 | 34.8 | 1.0 |
| 1.91 | 79.7 | 0.174 | 6.01 | 7.52 | 57.9 | 3.79 | 36.8 | 1.01 | 42.2 | 1.06 |
| 2.08 | 80.4 | 0.176 | 7.47 | 7.50 | 71.3 | 3.81 | 45.2 | 1.09 | 52.0 | 1.14 |

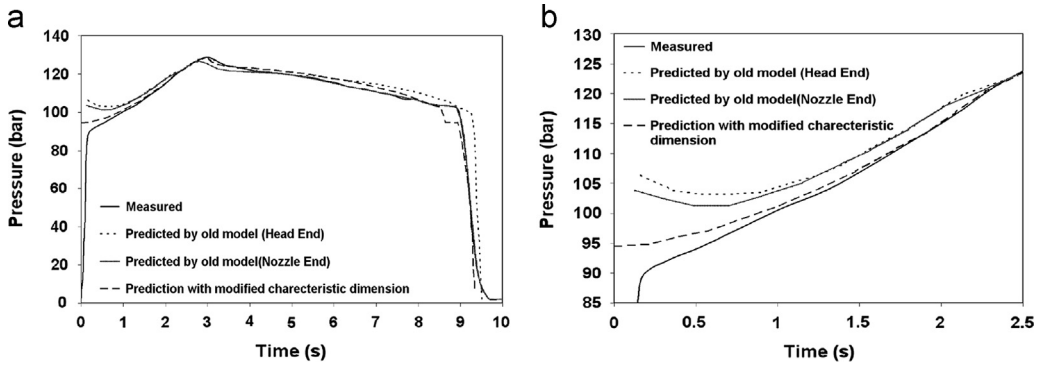


**Fig. 9.** Predicted and measured chamber pressures (a) full burn time (b) zoomed view to show the effect of modified model (Motor-1).

As can be noted from Table 3, the difference between the estimates of erosive burning ratio ($\eta$) is non-insignificant. The quantity, $\eta'$ refers to the value of erosive burning choosing the hydraulic diameter, $d_h$ that was adopted in the earlier work [1]. In order to determine the influence of this difference on the calculation of pressure time curve and verifying it against measured values, calculation was made using an internal ballistic code that solves the gas dynamics of internal flow in a step-wise approach. The results of head end chamber pressures with time for a throat diameter of 44.5 mm (which erodes to 47.4 mm linearly after 3 s) using both the estimation procedures (with $\eta$ and $\eta'$) are set out along with experimentally measured data in Fig. 9(a). As can be seen, the estimation with modified characteristic dimension shows a behavior close to the experimental result. A further confirmation of the weak influence of erosive burning in this motor has been obtained by a small difference between the head end and aft end pressures (less than 0.05 MPa). This observation can be seen more clearly in the zoomed view of the comparison in the initial phase of the operation as shown in Fig. 9(b). The predictions of the pressure time curve along with the test data for Motor-2 is presented in Fig. 10 for the early period where erosive burning effects can be expected to be significant. A close match with the experimentally observed head end pressure is noticed for the prediction with the modified erosive burning model.

It may be useful to examine the variation of the erosive burning related features. Fig. 11 carries the plot of the total burn rate including the erosive component along the grain for the choice of characteristic diameter based on hydraulic mean diameter as well as the new definition. Though there are

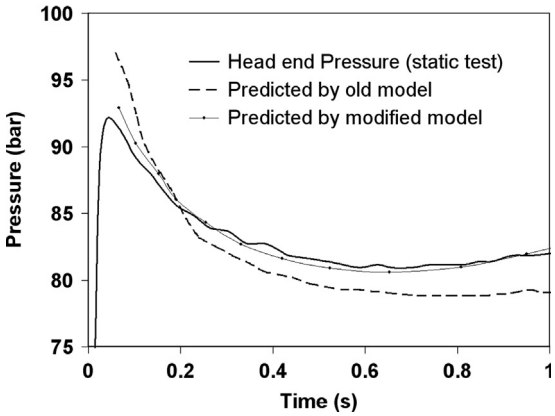


**Fig. 10.** Zoomed view of measured and predicted chamber pressures using the old and modified versions of the erosive burning model (Motor-2).

differences, they are not significant. This allows one to simplify the approach to including erosive burning features into the ballistic calculation. One does not need to deal with the variation of the burn rate along the periphery of a complex shape (like Finocyl or star), but use the approach of treating the characteristic dimension, $d_o$ as $P/\pi$ instead of 4 $A_p/P$ and obtain a closer approximation to the actual pressure–time curve in complex geometries.

## 6. Conclusions

This paper extends the work on the universal law for erosive burning by defining the characteristic length, $d_0$ required to deal with grain shapes other than cylinders. The

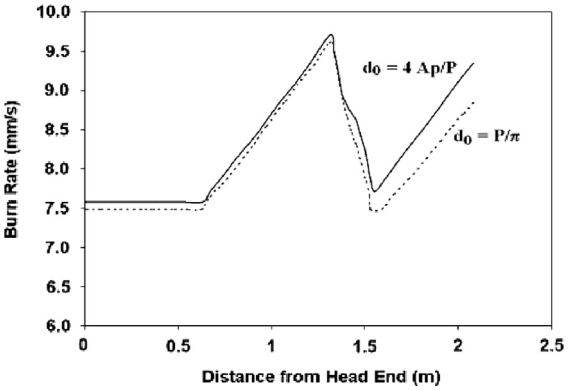


**Fig. 11.** The variation of burn rate (including the erosive burning) with the distance from head end with the two definitions of characteristic dimension (Motor-1).

results of flow velocity and wall shear stress from three dimensional steady flow calculations have been utilized to evolve a simple way of accounting for the effects of complex flows on erosive burning. The first simple approach that may be adequate in most cases is to consider $d_0 = P/\pi$ instead of $4\,A_p/P$. This preserves the earlier approach for cylindrical grains and extends to other grain shapes. If however, more complex accounting of regression of complex geometry is called for, a linear reduction in the heat flux along the propellant surface using the equation given in this paper along with blocking effect will be necessary.

## Acknowledgement

Authors are grateful to Dr. B. S. Subhash Chandran, Dr. K.K. Rajesh and team of DRDL for providing the geometrical details of rocket motors and useful inputs for the numerical simulations.

## References

[1] H.S. Mukunda, P.J. Paul, Universal behavior in erosive burning of solid propellants, Combust. Flame 109 (1997) 224–236.
[2] H. Hasegawa, M. Hanzawa, S. Tokudome, M. Kohno, Erosive burning of aluminized composite propellants: X-Ray absorption measurement, correlation, and application, J. Propul. Power 22 (5) (2006) 975–983.
[3] L.A. Dickinson, F. Jackson, A.L. Odgers (1960), Erosive burning of polyurethane propellants in rocket engines, in: Proceedings of the Eighth International Symposium on Combustion, Williams and Wilkins, Baltimore, MD, pp. 754–759.
[4] V.D. Topalian, J. Zhang, T.L Jackson, A.H.G. Isfahani, Numerical study of erosive burning in multidimensional solid propellant modeling, J. Prop. Power 27 (2011) 811–821. (August).
[5] Serraglia, F., Favini, B., di Giacinto, M., Neri, A., Gasdynamic features in solid rocket motors with finocyl grain during ignition transient, in: Proceedings of the Fifth European Symposium on Aerothermodynamics for Space, Nov. 2004, ⟨http://adsabs.harvard.edu/full/2005ESASP.563.479S⟩.
[6] F.A.Williams, M. Barrere, N.C. Huang, Erosive Burning, Fundamental Aspects of Solid Propellant Rocket, AGARD, AGARDograph 116, 395–456, 1969.
[7] ICEM CFD-11, Installation and Overview, January—2007.
[8] ANSYS CFX, Release 11.0, Ansys Inc. Release Notes, January—2007.
[9] S. Gordon B.J. McBride (1996): Computer Program for Calculation of Complex Chemical Equilibrium Compositions and Applications—II Users Manual and Program Description, NASA RP-1311.